



Flares, Rotation, Activity Cycles, and a Magnetic Star–Planet Interaction Hypothesis for the Far-ultraviolet Emission of GJ 436

R. O. Parke Loyd¹ , P. C. Schneider^{2,3} , James A. G. Jackman⁴ , Kevin France⁵ , Evgenya L. Shkolnik⁴ , Nicole Arulanantham⁶ , P. Wilson Cauley⁵ , Joe Llama⁷ , and Adam C. Schneider^{8,9}

¹Eureka Scientific, 2452 Delmer Street Suite 100, Oakland, CA 94602-3017, USA; astroparke@gmail.com

²Hamburger Sternwarte, Gojenbergsweg 112, D-21029, Hamburg, Germany

³Scientific Support Office, Directorate of Science, European Space Research and Technology Center (ESA/ESTEC), Keplerlaan 1, 2201, AZ Noordwijk, The Netherlands

⁴School of Earth and Space Exploration, Arizona State University, 781 E. Terrace Mall, Tempe, AZ 85287, USA

⁵Laboratory for Atmospheric and Space Physics, Boulder, CO 80309, USA

⁶Space Telescope Science Institute, 3700 San Martin Drive, Baltimore, MD 21218, USA

⁷Lowell Observatory, 1400 West Mars Hill Road, Flagstaff, AZ 86001, USA

⁸United States Naval Observatory, Flagstaff Station, 10391 West Naval Observatory Road, Flagstaff, AZ 86005, USA

⁹Department of Physics and Astronomy, George Mason University, MS3F3, 440 University Drive, Fairfax, VA 22030, USA

Received 2022 October 29; revised 2023 February 3; accepted 2023 February 12; published 2023 March 7

Abstract

Variability in the far-ultraviolet (FUV) emission produced by stellar activity affects photochemistry and heating in orbiting planetary atmospheres. We present a comprehensive analysis of the FUV variability of GJ 436, a field-age M2.5V star ($P_{\text{rot}} \approx 44$ days) that is orbited by a warm Neptune-sized planet ($M \approx 25 M_{\oplus}$, $R \approx 4.1 M_{\oplus}$, $P_{\text{orb}} \approx 2.6$ days). Observations at three epochs from 2012 to 2018 span nearly a full activity cycle, sample two rotations of the star and two orbital periods of the planet, and reveal a multitude of brief flares. From 2012 to 2018, the star's 7.75 ± 0.10 yr activity cycle produced the largest observed variations, $38\% \pm 3\%$ in the summed flux of the major FUV emission lines. In 2018, the variability due to rotation was $8\% \pm 2\%$. An additional $11\% \pm 1\%$ scatter at a cadence of 10 minutes, which is treated as white noise in the fits, likely has both instrumental and astrophysical origins. Flares increased time-averaged emission by 15% over the 0.88 days of cumulative exposure, peaking as high as $25\times$ quiescence. We interpret these flare values as lower limits given that flares too weak or too infrequent to have been observed likely exist. GJ 436's flare frequency distribution at FUV wavelengths is unusual compared to other field-age M dwarfs, exhibiting a statistically significant dearth of high-energy ($>4 \times 10^{28}$ erg) events, which we hypothesize to be the result of a magnetic star–planet interaction (SPI) triggering premature flares. If an SPI is present, GJ 436 b's magnetic field strength must be $\lesssim 100$ G to explain the statistically insignificant increase in the orbit-phased FUV emission.

Unified Astronomy Thesaurus concepts: [Stellar activity \(1580\)](#); [Exoplanets \(498\)](#); [Magnetic fields \(994\)](#); [Late-type dwarf stars \(906\)](#); [Ultraviolet astronomy \(1736\)](#); [M dwarf stars \(982\)](#); [Star-planet interactions \(2177\)](#); [Solar-terrestrial interactions \(2177\)](#); [Stellar rotation \(1629\)](#); [Stellar flares \(1603\)](#)

1. Introduction

GJ 436 is a nearby M2.5 V, $0.45 M_{\odot}$ star (Hawley et al. 2003; Knutson et al. 2011), which is well known for its lone Neptune-sized planet ($M = 25.4^{+2.1}_{-2.0} M_{\oplus}$, $R = 4.10 \pm 0.16 R_{\oplus}$; Butler et al. 2004; Gillon et al. 2007; Lanotte et al. 2014) that is actively losing atmospheric mass (Kulow et al. 2014; Ehrenreich et al. 2015). This planet is an upcoming target for atmospheric characterization by the James Webb Space Telescope (GTO programs 1177 and 1185; PI: T. Greene), and the system has undergone extensive spectroscopic observation at far-ultraviolet (FUV) wavelengths (France et al. 2013, 2016; dos Santos et al. 2019). These FUV observations provide an opportunity to investigate the variability of a field-age (Torres et al. 2008) partially convective M dwarf in high-energy emission across a wide range of timescales, from seconds to years. The data can probe variability as short-lived as stellar flares and as long-lived as stellar activity cycles. This information is relevant to

exoplanets, where variations in FUV irradiation affect the rates of photochemistry and heating in their atmospheres (e.g., Segura et al. 2007). Because M dwarfs are numerous and favorable for exoplanet observations (e.g., Shields et al. 2016), the constraints on FUV variability that are available for GJ 436 are broadly applicable to a large number of planets.

The GJ 436 system could be experiencing an interaction between the star and its single close-in planet. Many forms of star–planet interactions (SPIs) have been proposed, such as tidal suppression of activity, tidal spin-up, and shrouding by escaped planetary gas (Cuntz et al. 2000; Fossati et al. 2013; Pillitteri et al. 2014; Poppenhaeger & Wolk 2014). Of particular interest is a direct magnetic interaction with the planet that results in energy dissipation at the stellar surface, producing a hot spot that circles the stellar surface at the orbital period of the planet (Saur et al. 2013). For GJ 436, this is 2.64 days (Bourrier et al. 2018). Direct magnetic interactions themselves have many flavors, including particle precipitation from the reconnection of stellar and planetary fields, Alfvén wave dissipation, and triggering reconnections of stellar fields (Lanza 2015). For magnetic disturbances to reach the star, the Alfvén Mach number at the planet must be < 1 (Saur et al. 2013).

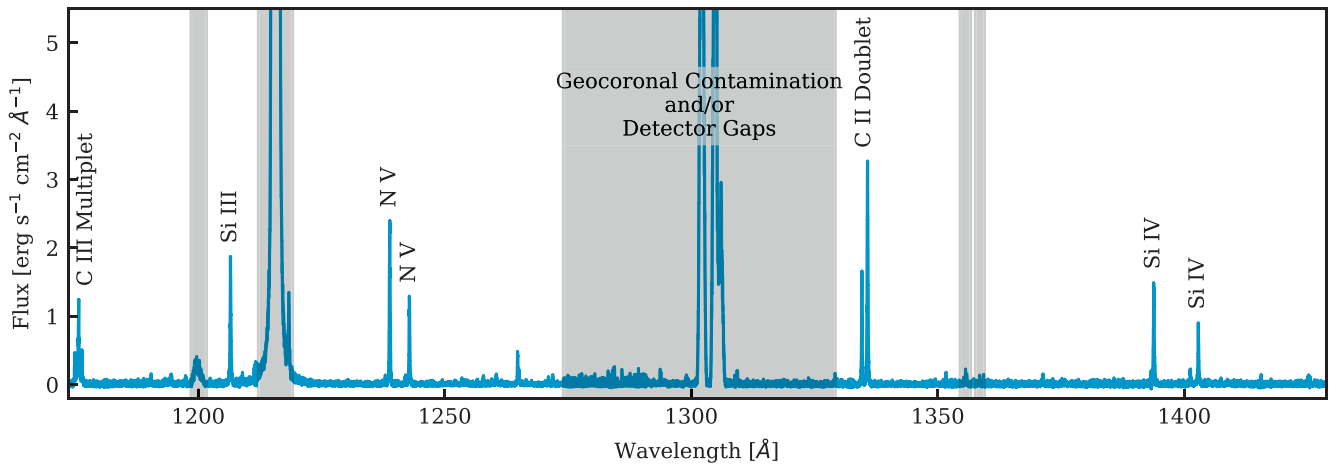


Figure 1. Coadded spectrum of GJ 436. The range of the plot matches that of the FUV₁₃₀ band. The gray regions delineate regions of airglow contamination and a detector gap that falls near 1300 Å that we masked from the FUV₁₃₀ band. The labels indicate the strong emission lines, which we also analyzed for variability, and the regions between the labeled lines and gray bands represent the pseudocontinuum.

Though difficult to predict, this could well be the case for GJ 436 b (see Section 3.5).

A number of past works have identified evidence of this kind of SPI in hot Jupiter systems (e.g., Shkolnik et al. 2008; Walker et al. 2008; Pagano et al. 2009; Cauley et al. 2019). Because the strength of the magnetic SPI, and hence the amplitude of its periodic signal, is controlled by the planetary magnetic field strength, this possibility provides the prospect of probing the magnetic field of GJ 436 b (Lanza 2015). With this in mind, we conducted targeted observations in 2017 and 2018 to sample the star’s FUV emission across the planetary orbital period.

In this paper, we report on a comprehensive variability analysis of GJ 436’s FUV emission and a search for a magnetic SPI. This work provides an independent replication of a similar analysis that was conducted as part of a transit study by dos Santos et al. (2019; hereafter, *ds19*). Their transit analysis confirmed the stability of the planet’s remarkable Ly α transit and demonstrated no significant transit in metal lines. Meanwhile, their variability analysis yielded evidence for rotational modulation in C II, Si III, and N V emission stable over several years, as well as magnetic cycle variations leading to optical, Ca II, and FUV variations consistent with changing spot coverage. In comparison to *ds19*, the present work adds a population study of the star’s flares, details of variability fits, and the results of an SPI search.

2. Methods

We analyzed all the available observations of GJ 436 made with the Cosmic Origins Spectrograph (COS) on board the Hubble Space Telescope (HST) that utilized the G130M grating. The observations originate from four programs that observed over three separate epochs spanning 5.5 yr: HST-GO-12464 (PI: K. France), 13650 (PI: K. France), 14767 (PI: D. Sing), and 15174 (PI: R. O. P. Lloyd). The data are aggregated under DOI: [10.17909/6p65-wg08](https://doi.org/10.17909/6p65-wg08). Details of the observations are available at the DOI link, where they can be downloaded.

The G130M grating covers wavelengths in the range 1150–1450 Å at a resolving power of 12,000–16,000. The detector is a photon counter, yielding event lists that can be arbitrarily binned in wavelength and time within the limits of the detector’s resolution. From these lists, we created flux-calibrated lightcurves, following the methodology presented in Lloyd & France (2014) and

Lloyd et al. (2018b; hereafter, *L18*). Figure 1 shows the observed band and Figure 2 indicates the quantity and duration of the data originating from the various observing programs.

We isolated the flux within several bands to analyze for variability. The largest of these was the FUV₁₃₀ band that was used in the flare analysis of M-dwarf stars by *L18*. Figure 1 plots the spectrum of GJ 436 within the FUV₁₃₀ band, created by coadding all exposures. As in *L18*, the regions masked in gray were excluded from the band, because they were contaminated by geocoronal airglow emission and, in the case of the mask near 1300 Å, were also affected by a gap between the two butted detectors used by COS. The coadded spectrum shown in Figure 1 does not exhibit this gap, because it was eliminated by dithering. We also analyzed the emission from ± 100 km s⁻¹ bands covering five strong emission lines and multiplets, C III, Si III, N V, C II, and Si IV, as labeled in Figure 1. These lines cover a formation temperature range of 4.5–5.2 in log₁₀(K), within the stellar transition region (Dere et al. 1997; Del Zanna et al. 2021). For multiplets, we summed the flux from all components. As a final band, we summed the flux between the lines, labeling this the “pseudocontinuum,” since it comprises both continuum sources as well as weak or undetected emission lines.

We identified flares in the data using the method described in *L18*, with some modifications. The algorithm identifies flares by isolating runs (series) of points above the mean value of the lightcurve that have an integrated energy that is at least 5 σ larger than the average run. It uses a maximum likelihood estimate for the mean, masking any previously identified flares. Chunks of data with gaps longer than 24 hr are processed separately, allowing for, e.g., variations in the mean due to rotation. The process of estimating the mean and identifying flares is iterated until convergence. Newly identified flares are masked with each iteration, to mitigate the upward bias in the mean produced by flares.

Rather than using the FUV₁₃₀ flux to identify flares, as in *L18*, we used the summed emission line fluxes. These lines are more sensitive to flares than the pseudocontinuum portions of the FUV₁₃₀ band. Including the pseudocontinuum added substantial noise, without substantially increasing the signal, reducing the sensitivity to flares. We also increased the span of the data that were masked around a flare, to start 120 s ahead of and extend to three times the length of each run of data that as identified as a flare.

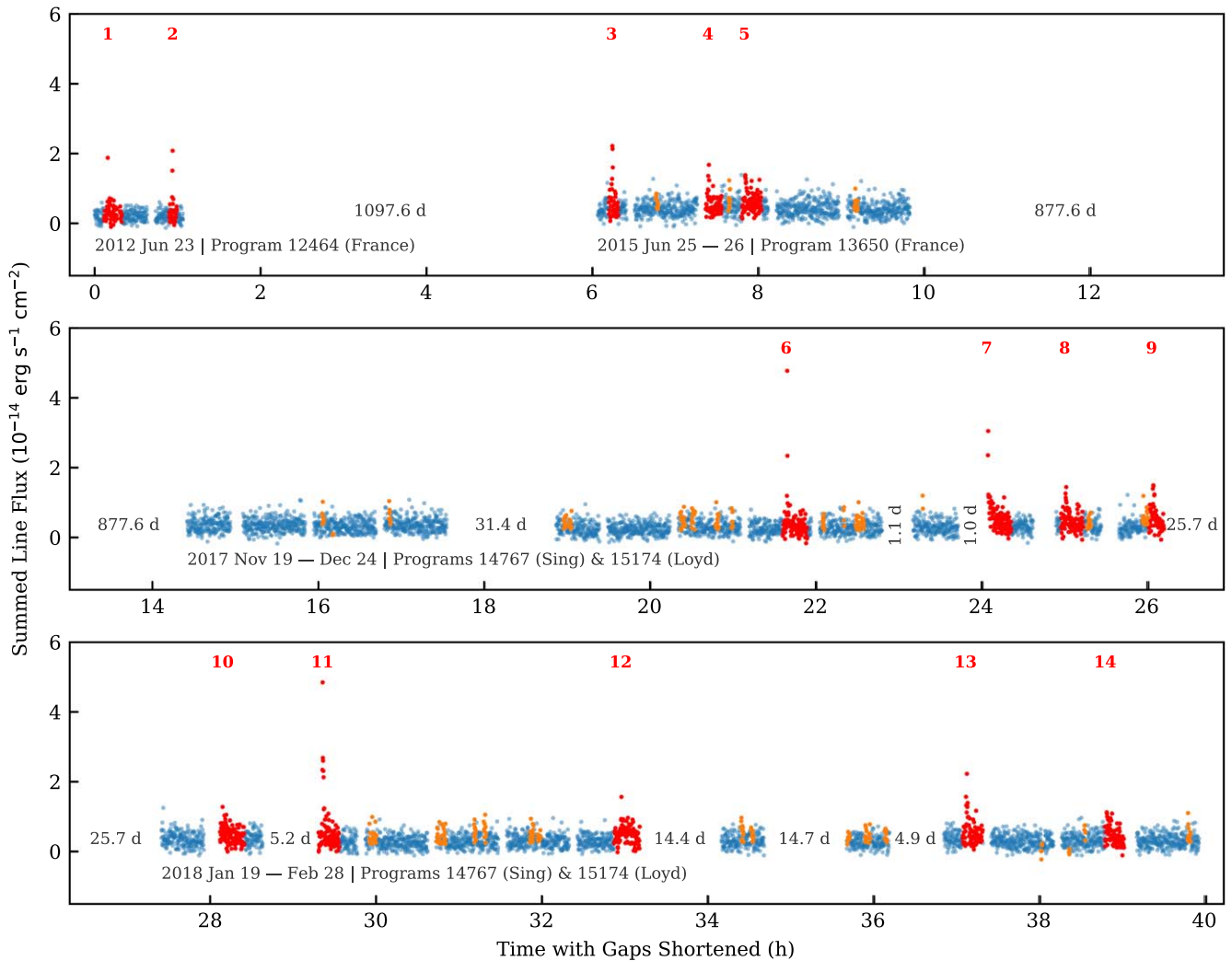


Figure 2. Lightcurve of the summed emission line flux at a 10 s cadence. We shortened the gaps in the data to a logarithmic scaling of their original lengths, as labeled in the plots. The labels below each epoch of data indicate the date range covered and the program(s) from which the observations originated. The red points indicate flares detected at $>5\sigma$, with assigned labels above them in red. The orange points indicate anomalous ($>3\sigma$) runs of data that were excluded when estimating the quiescence for the purpose of flare detection.

After identifying flares in the summed line flux, we measured the equivalent duration, energy, and peak flux of each flare in the FUV₁₃₀ band, to enable direct comparisons to the results of L18. The equivalent duration is the time that the star would have to spend in quiescence in order to emit the same energy in the same band as was emitted by the flare.

Having cleaned the data of flares, we binned the remaining data to ≈ 10 minutes and simultaneously fit for variability due to stellar activity cycles, rotation, a possible SPI, and a jitter term. We only used the 2017/2018 epoch of data to constrain rotation and SPI signals, because these were the only data that sampled across the planetary orbital period and the stellar rotation period without large gaps, where the phase and amplitude could have shifted. We did not mask or otherwise account for the planetary transits captured by the 2015 and 2017/2018 epochs, because there is no evidence of a transit in the FUV emission lines that we analyzed (ds19; Lavie et al. 2017; Loyd et al. 2017). We used the Markov Chain Monte Carlo (MCMC) code `emcee`¹⁰ (Foreman-Mackey et al. 2013) to sample the posterior distribution of the fit parameters, using

100 walkers to a factor of at least 100 times the autocorrelation length for the samples of each parameter, taken as the median of the values for all walkers.

The stellar rotation and activity cycle models were simple sine functions that were allowed to vary in amplitude and phase, but were fixed to a rotation period of 44.09 days and a cycle period of 7.75 yr, as measured from the optical data (described below). We fit this model to the data integrated to 10 minute bins with flares masked. After fitting the summed line fluxes, we used the posterior on the phase from that fit as a prior for the other bands with lower signal-to-noise ratios, to better constrain their variability amplitudes.

The jitter term was Gaussian white noise that was added in quadrature to the measurement uncertainty of each data point. This quantity effectively represented how much more scatter was present in the lightcurve than was expected from the measurement uncertainties, being analogous to the excess noise metric of Loyd & France (2014). However, we used longer time bins of 10 minutes, instead of the 1 minute bins used by Loyd & France (2014), to offset the faintness of GJ 436, which was the fifth faintest star among the 42 analyzed in Loyd & France (2014). We allowed the standard deviation of the added

¹⁰ <https://emcee.readthedocs.io/en/stable/>

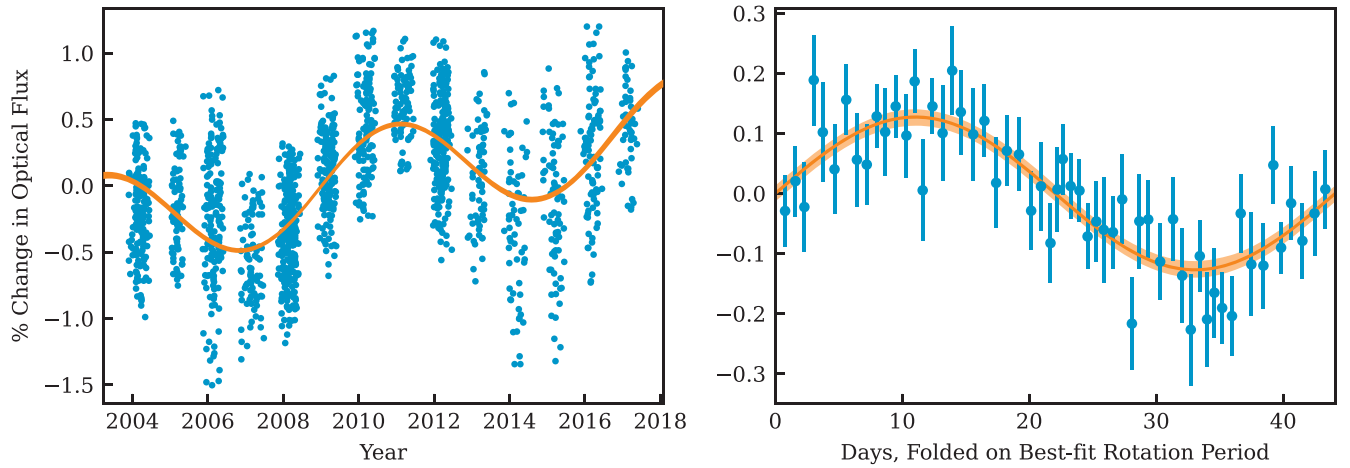


Figure 3. Our fit to the Strömgren $(b + y)/2$ photometry from Lothringer et al. (2018), mimicking their Figure 1. Left: data with a sinusoidal fit to the 7.75 ± 0.10 yr activity cycle period, with the linear trend overlaid. The line thickness represents the uncertainty of the fit. Right: data with the activity cycle sinusoid and linear trend subtracted, folded onto the best-fit rotation period of 44.09 ± 1.16 days and binned by groups of 30. The rotation model sinusoid is overlaid, with the translucent region representing the uncertainty of the fit. The error bars show the sample errors on the means of the binned points.

noise to vary between epochs, resulting in three separate white noise parameters.

To fit for a possible magnetic SPI, we assumed a truncated sine model, as was done for Ca II H and K in Shkolnik et al. (2003, 2008). This model approximates the appearance of a bright optically thick spot of constant flux, with a viewing angle that shifts as it traverses the visible stellar hemisphere. However, FUV line emission within a hot spot might not be optically thick. If the emission should originate from an optically thin slab of plasma, being emitted isotropically, then the flux would be constant once the slab emerged from behind the stellar disk (e.g., Toriumi et al. 2020). To allow for this possibility, we added a shape parameter, α , to the truncated sin model, yielding a model of the form

$$F = \begin{cases} 0, & \sin \phi \leq 0 \\ \sin^\alpha \phi, & \sin \phi > 0 \end{cases} \quad (1)$$

where

$$\phi = \frac{2\pi}{P_{\text{orb}}} t + \Phi. \quad (2)$$

A is the amplitude, P_{orb} is the planetary orbital period of 2.64 days (Bourrier et al. 2018), and Φ is a phase offset. As $\alpha \rightarrow 0$, the function approaches a top hat, representative of the case where the hot spot emission is optically thin and the observed flux simply depends on whether the spot is visible or not. This ad hoc parameterization allowed the code to explore sinusoidal, top hat, and intermediate solutions. We fit this model to the data with flares included, because they could be triggered by an SPI that is simultaneous with the rotation and cycle fits, but with a separate jitter term. An initial run indicated that only upper limits would result. These limits could be unreasonably large should we allow the phase to vary freely, since the sampler could place the signal peak in a data gap. To provide a reasonable upper limit, we fixed the signal to be in phase with the orbit. Although phase offsets likely occur for an SPI-induced hot spot, they cannot be easily predicted

(Lanza 2013), and we consider a fixed-phase fit reasonable for an order-of-magnitude upper limit.

To provide a consistent comparison to the optical variability of GJ 436, we also analyzed the photometry in the Strömgren b - and y -band filters, described in Lothringer et al. (2018). We used the same techniques outlined above, but included the rotation period and the slope and intercept for a linear rise in flux as additional free parameters. In contrast to Lothringer et al. (2018), we fit the $(b + y)/2$ photometry in flux rather than magnitude space. We set the priors for the period of the rotation sinusoid to be < 365 days, the period of the activity cycle sinusoid to be > 365 days, and all amplitudes to be ≥ 0 . These priors did not prove restrictive. Figure 3 shows the results of this fit.

3. Results and Discussion

3.1. Flares

We identified 14 flares in the data, which are shown in the context of the entire data set in Figure 2. Table 1 gives the properties of these flares in the FUV₁₃₀ band, enabling a comparison to L18, as well as the summed line fluxes that are used to identify the flares and are shown in the figures. Most flares exhibit distinct peaks. Event 7 (and possibly also event 10) appears to be the decay phase of a flare that began prior to the start of an exposure. Events 5 and 14 do not exhibit clear peaks and, despite passing the statistical cut, could be false positives. We cannot definitively explain these flux increases. One possibility is that they are manifestations of magnetoacoustic waves or wave interference, which produce minute timescale variations in the transition region emission on the Sun, although it is unclear whether these variations significantly modulate disk-integrated emission (Sangal et al. 2022). Similar variations with greater amplitudes that stand out well above the noise have been observed on a young M star by Lloyd et al. (2018a). Another possible explanation is that these anomalies are conglomerations of weak flares.

The flares exhibited by GJ 436 are frequent, yet they are of unusually low energy. Figure 4 shows the cumulative flare frequency distribution (FFD) of the observed flare energies and equivalent durations (a metric of flare energy that is normalized

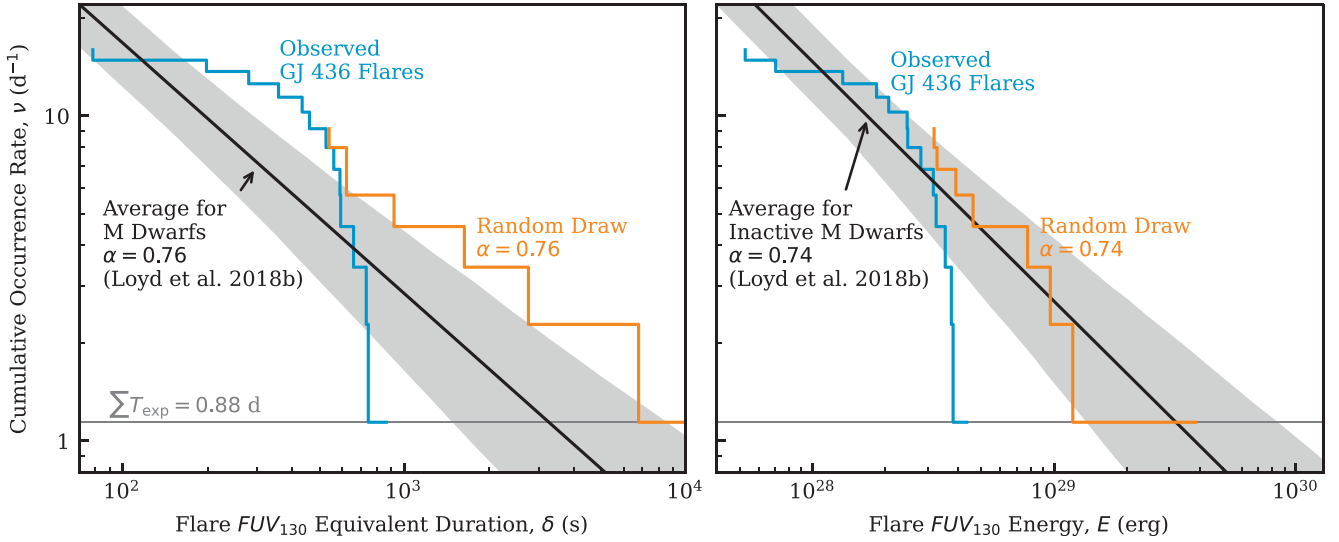


Figure 4. Cumulative frequency distribution of the GJ 436 flares in the FUV₁₃₀ band. The gray regions give uncertainty envelopes from fits to a compendium of M-dwarf flares in L18. To highlight the cliff in the GJ 436 flares, the figure also shows random draws of event equivalent durations and energies, assuming the same number of events above 500 s and 2.5×10^{28} erg and an inverse power-law slope, α , equal to the median observed by L18. The gray horizontal line represents the limit where one event would be expected to occur within the cumulative observing time.

Table 1
FUV Flares Detected from GJ 436

Summed Lines (Used to Identify Flares and Plotted in Figures 2 and 7)				FUV ₁₃₀ Band (per L18)					
δ s	E 10^{28} erg	F_{peak} 10^{-14} erg s ⁻¹ cm ⁻²	$\frac{F_{\text{peak}}}{F_q}$ ^a	δ s	E 10^{28} erg	F_{peak} 10^{-14} erg s ⁻¹ cm ⁻²	$\frac{F_{\text{peak}}}{F_q}$ ^a	t_{peak} MJD	No. ^b
1514 ± 130	3.76 ± 0.26	4.85 ± 0.67	23.2 ± 6.0	745 ± 120	3.76 ± 0.49	6.70 ± 0.82	16.1 ± 5.5	58142.88	11
1419 ± 118	3.52 ± 0.28	1.57 ± 0.38	8.2 ± 2.7	863 ± 129	4.35 ± 0.61	1.93 ± 0.54	5.4 ± 2.3	58143.15	12
1337 ± 112 ^c	3.68 ± 0.27	3.05 ± 0.53	13.6 ± 4.0	660 ± 90	3.82 ± 0.51	3.63 ± 0.68	8.1 ± 1.8	58110.89	7
1018 ± 117	2.29 ± 0.24	4.77 ± 0.66	25.1 ± 5.2	594 ± 111	2.81 ± 0.52	5.99 ± 0.81	15.4 ± 2.7	58108.72	6
1001 ± 95	2.92 ± 0.25	2.23 ± 0.46	9.7 ± 2.9	591 ± 97	3.16 ± 0.50	2.66 ± 0.65	6.7 ± 2.1	58177.33	13
884 ± 99	2.43 ± 0.26	1.44 ± 0.37	7.0 ± 2.4	562 ± 106	3.25 ± 0.61	2.55 ± 0.82	6.0 ± 2.0	58111.42	8
776 ± 87	2.14 ± 0.22	1.49 ± 0.37	7.2 ± 2.5	357 ± 86	2.07 ± 0.49	2.26 ± 0.59	5.4 ± 1.5	58111.70	9
663 ± 98	1.15 ± 0.17	1.88 ± 0.42	13.3 ± 3.0	732 ± 173	1.84 ± 0.39	2.26 ± 0.58	11.2 ± 5.2	56101.31	1
646 ± 92	2.14 ± 0.28	1.28 ± 0.34	5.4 ± 2.3	434 ± 89	2.48 ± 0.51	2.21 ± 0.54	5.4 ± 1.3	58137.65	10
627 ± 74	2.51 ± 0.28	1.38 ± 0.36	4.9 ± 1.9	527 ± 75	3.54 ± 0.50	2.23 ± 0.54	4.8 ± 1.1	57199.12	5
626 ± 85	1.82 ± 0.24	1.13 ± 0.33	5.4 ± 2.0	460 ± 104	2.47 ± 0.54	2.16 ± 0.60	5.6 ± 1.9	58177.46	14
476 ± 71	0.83 ± 0.12	2.08 ± 0.43	14.6 ± 3.0	280 ± 131	0.70 ± 0.28	2.69 ± 0.61	13.2 ± 5.9	56101.37	2
395 ± 64	1.58 ± 0.24	1.68 ± 0.40	5.8 ± 2.1	78 ± 67	0.53 ± 0.45	1.97 ± 0.59	4.3 ± 1.3	57199.10	4
317 ± 55	1.27 ± 0.19	2.22 ± 0.44	7.3 ± 2.5	198 ± 47	1.33 ± 0.31	3.00 ± 0.57	6.1 ± 1.2	57198.99	3

Notes.

^a The ratio of the peak flux to the quiescent flux.

^b The chronological order of the flares, corresponding to the numerical labels in the figures.

^c The exposure began after the start of the flare, as indicated by the lack of any data points below the quiescent level prior to the peak. The energy and equivalent duration are lower limits.

by the star’s quiescent emission) in comparison with FFDs that are made by combining observations of 10 M dwarfs in the same FUV₁₃₀ band (L18). Although the L18 FFDs incorporate the 2012 and 2015 epochs of the GJ 436 data, they make up <10% of the data, so they will not significantly bias the comparison. The flattening of the GJ 436 FFD at low energies represents the event detection limit.

The GJ 436 FFD does not appear to follow the “M-dwarf average” power law from L18, since a cliff in the FFD is exhibited toward large equivalent durations (δ) and energies. Within the cumulative exposure of 0.88 days, the equivalent

duration and energy of the strongest expected event would be ≈ 3000 s and $\approx 3 \times 10^{29}$ erg (where the L18 FFD lines intersect the 0.88 day⁻¹ occurrence rate in Figure 4), but the strongest observed event is several times weaker. The observed flare rate is not affected by exposure gaps, since flares are effectively random in time (Wheatland 2000). The observed energies can be underestimated when gaps cut off events (such as event 7), but the bias that this introduces is below the statistical uncertainty resulting from a small sample size (see the injection recovery tests with gappy data in Appendix C of L18).

To test the possibility that the FFD cliff is the result of a small sample size, we randomly drew flares from the L18 equivalent duration FFD for comparison. In 900,000 trials, 10% yielded no flares with equivalent durations beyond the cliff. However, of this 10%, most trials produced fewer total flares. When we considered only trials that yielded at least as many flares with $\delta > 500$ s as GJ 436 (180,000 trials yielding ≥ 8 flares), only 0.02% produced events that were no more extreme than those observed from GJ 436. In other words, if GJ 436's FFD were to be consistent with the FFDs of other M dwarfs, it is highly unlikely that it could yield as many flares as observed, yet produce none with equivalent durations > 860 s. This implies that GJ 436's FFD is steeper than is typical. A power-law fit to the $8\delta > 500$ s events yields an exponent < -2 , well below the 0.76 ± 0.1 that is typical for M dwarfs (L18), although the fit is poor due to the low number of events. We hypothesize that this unusual FFD is the result of a magnetic SPI (Section 3.5).

To investigate whether GJ 436 is able produce more energetic flares over longer timescales, we searched 43 days of optical observations by the Transiting Exoplanet Survey Satellite (TESS). The presence of a flare in those data would have been evidence against the cliff in UV flare energies being a real feature. However, we found no flares in the TESS data. Because flares produce very low contrasts at optical wavelengths (e.g., MacGregor et al. 2021), the possibility remains that flares with large UV energies occurred, but their optical signals were buried in the noise of the TESS time series.

3.2. Rotation

Based on our fits to the data sampling two and a half stellar rotation periods during the 2017/2018 epoch, we detected stellar rotational modulation at $> 2\sigma$ in each band and 4.3σ in the summed line flux, with typical amplitudes spanning 5%–13%. Figure 5 shows these fits and Table 2 gives the fit parameters. MCMC chains of the fits and corner plots are available upon request to the corresponding author.

Taking into account the inclination of the star, the rotational variability can provide some insight into the net contrast of active regions. Bourrier et al. (2022) measured the star's spin axis as being inclined by $35.7^{+5.9}_{-7.6}$ relative to the line of sight.¹¹ At this inclination, latitudes beyond $\pm 54.3^\circ$ are always visible for one pole and invisible for the other. Granzer et al. (2000) found that active regions mostly occur within $\pm 54.3^\circ$ for slowly rotating M dwarfs. Therefore, most of GJ 436's active regions likely contributed to the observed variability, albeit with an apparent area foreshortened by the inclination.

ds19 analyzed the same FUV observations for rotational modulations. They only found the rotational modulation of the individual emission lines to be significant if they included the 2015 observations under the assumption, justified by optical observations (Bourrier et al. 2018), that the signal phase did not shift between the 2015 and 2017/2018 epochs. In our analysis, summing the emission line fluxes resulted in a $> 4\sigma$ measurement of the rotation signal amplitude, without needing the 2015 data. Regardless, we consider the rotational modulation of the FUV emission as more likely present than absent, given the signs of magnetic activity on GJ 436 and the rotational modulation of the UV emission due to magnetic activity on

the Sun (Toriumi et al. 2020). The ds19 fits yielded rotational amplitudes of roughly 15% in C II and Si III and 10% in N V. Our fits yielded lower levels of rotational variability (Table 2), likely because, in contrast with ds19, we did not include the higher fluxes of the 2015 epoch when fitting for rotation, due to concerns that the phase and amplitude could have shifted between the epochs.

We tested whether the FUV data could recover the rotation period of the star if we included the rotation period as a free parameter in the variability fit. In this case, the MCMC sampler identified multiple peaks in the posterior for the rotation period, with the two strongest at $21.3^{+0.2}_{-1.1}$ days and 6.69 ± 0.04 days (Figure 5, second panel), and only a weak peak in the vicinity of 44 days. The amplitudes of the short-period signals were greater than the fixed-period fit, but within 2σ . The multiple modes could be harmonics of the longer optical period, perhaps indicating that multiple longitudes of enhanced activity are contributing to the FUV variability.

In comparison to the FUV emission, the variability in the broadband optical emission is $\sim 0.1\%$. Our sinusoidal fit to the optical data (Figure 3) yielded a rotation period of 44.09 ± 1.16 days, with the zero phase occurring at JD 2455484.47 ± 0.73 (decimal year 2010.7862 ± 0.0020), with an amplitude of $0.127\% \pm 0.013\%$, consistent with the results of Bourrier et al. (2018) and Lothringer et al. (2018). In contrast, rotation measurements made using Ca II H and K and H α suggest periods nearer to 40 days (Suárez Mascareño et al. 2015; Kumar & Fares 2023). A rotation period within the 40–45 days range is typical of a field-age M dwarf with a mass $\approx 0.45 M_\odot$ (Bourrier et al. 2018; Newton et al. 2018). If the rotational variability is due to dark spots, the star should appear redder during optical lows, but Lothringer et al. (2018) could not detect this, suggesting that the variability could be dominated by faculae.

The phase difference between the UV and optical rotation curves encodes information about the surface structure of the stellar activity. If the rotation signals result from optically bright faculae that are co-spatial with FUV plage, then the two should be in phase. Alternatively, if optically dark spots that are co-spatial with FUV plage are responsible, then the two curves should be 180° out of phase.

In this case, however, a clear comparison of the UV and optical phases is precluded by the possibility of phase shifts in the optical rotation signal. The optical variability fit assumes a static phase over the 14 yr of data, a span that covers two activity cycles. Although the data, folded onto the best-fit period, show convincing modulation (Figure 3), hidden phase shifts over the 14 yr span could be present, particularly if the signal is dominated by only one or a few short periods of high variability.

To investigate possible shifts in the optical phase, we isolated 3 yr sections of the optical data, sampling the extrema of the activity cycle (2006–2008, 2010–2012, and 2013–2015). The fits to data near optical minima recovered the same 44 day period, with a larger amplitude near the 2014 minimum (0.27% versus 0.13%) and large uncertainties in phase allowing for shifts as high as 123° (1σ) from 2007 to 2014, which could affect an FUV–optical comparison. The fit to the data near the 2011 maximum did not clearly recover the 44 day period, yielding multiple modes in period and phase, all with amplitudes near 0.9%. The unclear period and lower-variability amplitude near the 2011 maximum could result from a lower

¹¹ The flipped inclination of 144.2° is equally probable, but does not influence our interpretation.

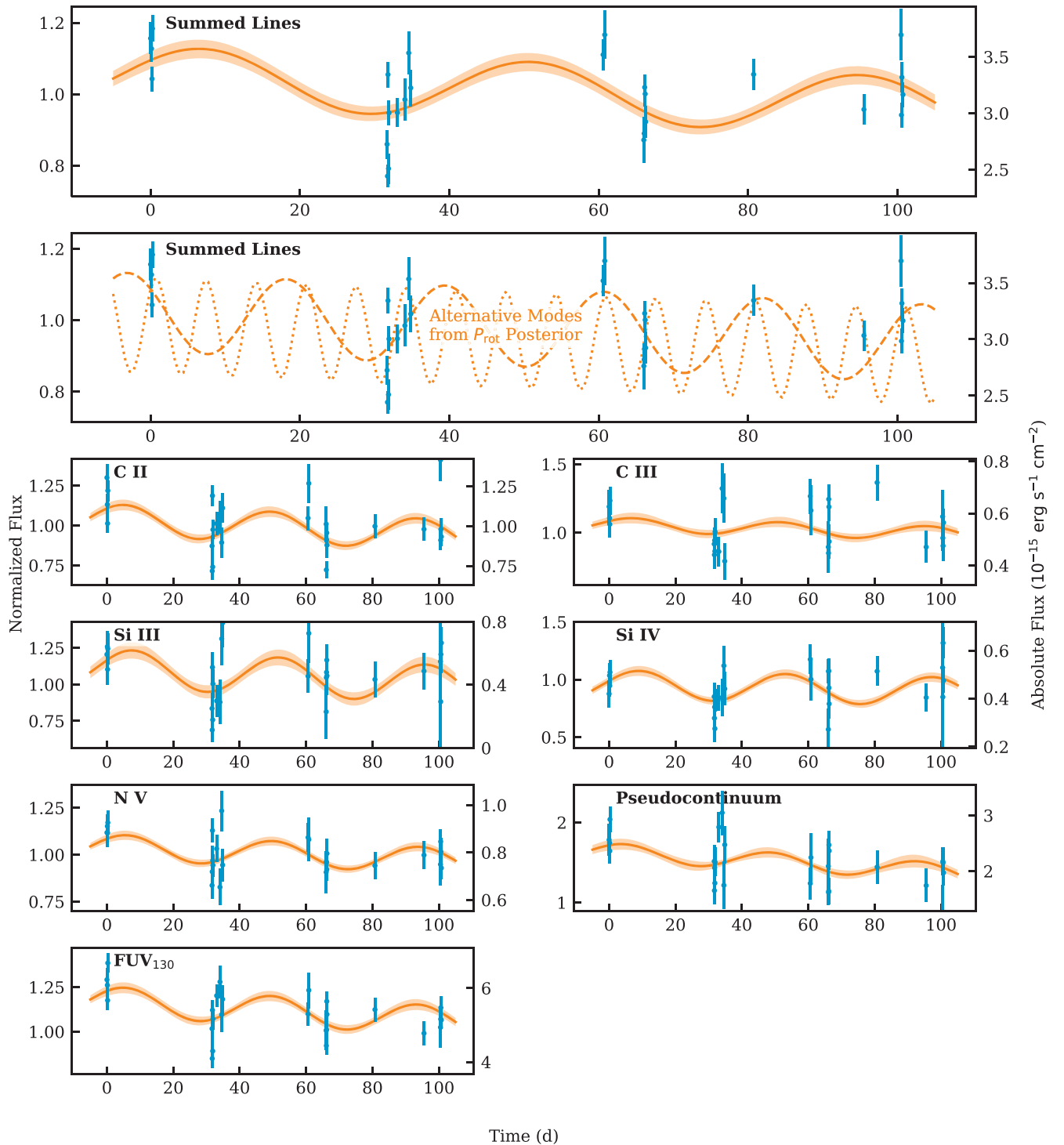


Figure 5. Fits to the rotational modulations of the flux in each of the analyzed bands during the 2017/2018 epoch of observations. The data have been cleaned of flares. The fits were made to data binned at a 10 minute cadence, but to minimize clutter, the plotted data are binned to the full exposure length (typically around 45 minutes). The fits corresponding to alternative periods are shown as the dotted and dashed lines in the second panel from the top (see the text). The slight downward trends in the UV fits are due to the simultaneous fits to the activity cycle.

activity level (fewer or weaker spots/faculae), a more homogeneous distribution of spots/faculae across the star, cancellations of spots by faculae, or any combination of the above. Since the 2017/2018 FUV observations occurred near the subsequent optical maximum, they could also be affected by reduced or more spatially homogeneous activity.

We also attempted to fit TESS data from the two available visits, sectors 22 and 49, observed in 2020 March and 2022

March, each only lasting for about half of the stellar rotation period. Separate fits to each did not reveal clear rotation signals or phase constraints. Higher-precision optical data are necessary to probe signal shifts over time.

Toriumi et al. (2020) provide solar context for how rotational variations, resulting from spots and faculae, manifest at optical versus UV wavelengths. By isolating periods where only a single active region was visible, they found that the variability

Table 2
Fits to the Variability in the FUV Emission Lines

Band	Mean Flux 10^{-16} erg s $^{-1}$ cm $^{-2}$	Cycle Amplitude %	Cycle t_0^a yr	Rotation Amplitude %	Rotation t_0^a d	SPI Amplitude %	Excess Noise ^b %
Summed Lines	$31.92^{+0.59}_{-0.74}$	$37.5^{+3.3}_{-3.0}$	$3.905^{+0.079}_{-0.075}$	$8.1^{+2.1}_{-1.6}$	-2.1 ± 1.5^c	<9.2	$10.8^{+1.5}_{-1.1}$
C II	$10.01^{+0.35}_{-0.29}$	$41.9^{+6.2}_{-3.8}$	3.86 ± 0.10	$9.5^{+2.6}_{-2.2}$	$-3.7^{+1.2}_{-1.1}$	<7.9	$13.6^{+2.4}_{-1.6}$
C III	$5.25^{+0.32}_{-0.27}$	$30.4^{+9.2}_{-9.5}$	$4.04^{+0.18}_{-0.31}$	$4.8^{+3.1}_{-2.3}$	$-1.7^{+1.4}_{-1.5}$	<13	<12
Si III	$3.55^{+0.22}_{-0.16}$	$50.8^{+8.0}_{-9.5}$	$4.02^{+0.13}_{-0.15}$	$13.0^{+4.1}_{-3.7}$	$-1.2^{+1.2}_{-1.3}$	<16	$21.5^{+4.1}_{-3.0}$
Si IV	$4.74^{+0.31}_{-0.21}$	$29.1^{+8.7}_{-7.1}$	$3.66^{+0.17}_{-0.42}$	$12.5^{+3.0}_{-3.1}$	$0.1^{+1.1}_{-1.2}$	<11	$8.1^{+3.6}_{-5.3}$
N V	$7.89^{+0.23}_{-0.27}$	$30.3^{+6.8}_{-4.0}$	$3.95^{+0.11}_{-0.15}$	$6.7^{+1.8}_{-1.6}$	$-3.0^{+1.1}_{-1.2}$	<4.8	$6.9^{+1.9}_{-3.6}$
Pseudocontinuum	$14.4^{+1.5}_{-5.1}$	89^{+174}_{-13}	$4.538^{+0.052}_{-0.065}$	$11.7^{+7.8}_{-4.5}$	$-4.3^{+1.8}_{-1.4}$	<10	14^{+12}_{-8}
FUV ₁₃₀	$48.1^{+1.8}_{-3.3}$	47^{+16}_{-8}	$4.24^{+0.06}_{-0.11}$	$8.3^{+2.4}_{-2.0}$	-3.5 ± 1.2	<7.8	$10.7^{+2.1}_{-1.9}$

Notes.

^a The time at which the phase of the sin function reaches zero after 2018 January 1 00:00:00 UT (58119.0 MJD).

^b Additional white noise hyperparameter for the 2018 epoch, excluding flares.

^c Applied as a prior to the remaining fits.

in extreme UV (EUV) emission lines could either be in or out of phase with the optical variability. The determining factor was whether the brightened active region or its dimmed surroundings dominated. The dimming is caused by the heating of the surrounding plasma to higher temperatures, reducing the emission from lower-temperature lines. The variations in EUV emission also start earlier and end later than the optical variations, because the EUV emission originates above the photosphere, with the result that it is visible when photospheric active regions are hidden just beyond the limb. Finally, the EUV variations exhibit top hat-like shapes, due to low optical depths. GJ 436’s FUV variability could exhibit similar effects, though, unlike the transition region FUV lines that we analyzed, the most analogous EUV lines that were analyzed by Toriumi et al. (2020) included substantial flux from hotter, less dense coronal plasma.

3.3. Activity Cycles

The activity cycle of GJ 436 was measured by Lothringer et al. (2018) as having a period of roughly 7.4 yr, with an amplitude of 5 mmag (0.5%), at optical wavelengths. Our analysis of the same data yielded a period of 7.75 ± 0.10 yr and an amplitude of $0.376\% \pm 0.015\%$ (4 mmag), with a zero phase occurring at JD 2454826 ± 18 (decimal year 2008.982 ± 0.049). A long-term increase of $0.050\% \pm 0.003\%$ over the 14 yr span of observations is also present. The difference of 0.35 yr between our cycle period and that of Lothringer et al. (2018) is likely a systematic uncertainty, due to subjective analysis choices (using flux versus magnitude, the functional form of the long-term trend, the functional form of the cycle variability, the inclusion and form of a jitter term, etc.). An additional search for the star’s activity cycle signature in Ca II H and K, Na I, and H α activity indicators by Kumar & Fares (2023) yielded signals spanning 5.1–6.8 yr. All of the aforementioned values fall near the predicted value of 7.6 yr, based on the relationship between the activity cycle and the rotation period established by Suárez Mascareño et al. (2016). The simple sinusoidal shape of the activity cycle echoes that of field-age Sun-like stars, with weak faculae-dominated activity.

The three epochs of HST data span nearly a full activity cycle and show significant variability beyond what can be explained by stellar rotation, visit-to-visit systematic flux errors (<2%; James 2022), or excess noise (2%–4% when binned

over visits of two to five orbits). Fitting a sinusoid to these data, fixed to the period of the optical cycle, yields amplitudes of 30%–50%. The amplitude of the cycle variability in the pseudocontinuum stands out at $89^{+174}_{-13}\%$. We interpret this difference with caution because, on a pixel level, the flux in the pseudocontinuum was below the noise floor of COS and vulnerable to errors in the background subtraction and time-varying flat-field correction.

Similar to rotational variability, if optically dark, FUV-bright active regions explain this variability, then the optical and FUV activity cycles should be 180° out of phase (Reinhold et al. 2019). For GJ 436, the optical variability lags the FUV variability by $119^\circ \pm 6^\circ$ (Figure 6). dS19 found that the variations in the Ca II S-index were out of phase with the optical variations, though the constraint was not quantified.

The intermediate FUV–optical phase offset could indicate that GJ 436 is undergoing a transition from spot-dominated to faculae-dominated activity. Sun-like stars exhibit similar intermediate-phase offsets between their activity cycles in Ca II H and K and optical emission, as they transition from spot to faculae dominance (Reinhold et al. 2019) around a Rossby number of 1, similar to GJ 436’s Rossby number of 0.74 (Lloyd et al. 2021). A transitional state for GJ 436 could explain its mixed indications of spot- and faculae-driven variability.

Systematic unknowns could make a 180° FUV–optical phase difference possible. A global trend of about $7\% \text{ yr}^{-1}$ to the FUV emission would suffice, as would allowing the FUV cycle to vary in amplitude, with it being about half the value in 2018 as it was in 2012. Another option would be to interpret the 2012 and 2015 observations as sampling rotational minima, meaning that the average fluxes were higher at those epochs, which would shift the cycle curve to earlier times. The star’s increase in optical variability near 2015 (Section 3.2) could indicate larger FUV variations at that time. On the Sun, the amplitude of rotational variability waxes and wanes over the activity cycles at optical and EUV emission wavelengths (Fröhlich 2006; Woods et al. 2022; Llama 2023, private communication).

3.4. Excess White Noise

We included an excess white noise parameter (“jitter” term) in our fits, so that the MCMC sampler could explore an alternative to forcing the rotational, cyclic, or SPI signals to

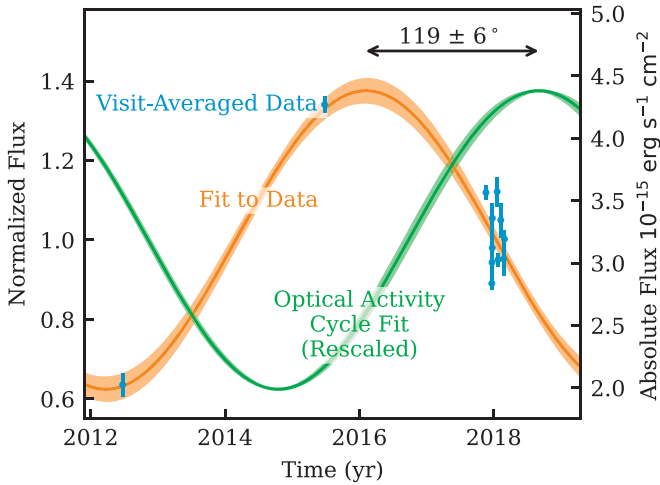


Figure 6. Summed line flux (blue points), binned by HST visit, across all three epochs of HST data, fit with a sinusoidal model for activity cycle variations (orange curve) fixed to the optical cycle period, and shown alongside the (rescaled) fit to the optical cycle (green curve), to compare phases.

produce the observed point scatter. The sampler identified excess white noise, in addition to other variability, at levels of 10%–20% in all bands, except C III. The amplitudes of excess noise and other variability were uncorrelated, i.e., increasing the noise did not require decreasing other variability, to obtain a similar goodness of fit.

Excess noise could come from a mixture of instrumental and astrophysical sources. A known instrumental source is the movement of fixed pattern noise when the position of the spectrum on the detector is shifted (by as much as 36 \AA , or 10% of the wavelength range) between observations. However, instrumental noise of this kind is unlikely to account for the entirety of the measured excess noise, given the 2% visit-to-visit accuracy of COS (James 2022). Astrophysical sources could include undetected flares, “transition region bombs,” shocks initiated by convective motions, and others (Lloyd & France 2014).

Excess noise, instrumental or astrophysical, limits the detectability of planet b’s transit in FUV emission lines, aside from Ly α (Lavie et al. 2017; Lloyd et al. 2017; dS19). Integrated to a 1 hr cadence (and assuming a flat power spectral density), the noise level is $5.8\% \pm 0.8\%$ in the emission from the least-ionized ion that we analyzed, C II. Lloyd & France (2014) estimated excess noise with an analytical method and a 60 s cadence, using only the 2012 data, and found values equating to $2.5\% \pm 1.4\%$ in C II at a 1 hr cadence.

3.5. Magnetic SPI

To search for an SPI, our HST program (HST-GO-15174) was designed to add 8 points, sampling across the orbital phase of GJ 436 b. The data augmented the transit investigations of program HST-GO-14767. This sampling was motivated by a peak in the N V emission of GJ 436, in phase with the planet transit during the 2015 epoch.

We found no detectable evidence of an SPI, in the form of variations in the emission from GJ 436, in N V or any other line phased with the planetary orbit. Our simultaneous fits limit SPI variability in the summed line flux to $<9.4\%$ (2σ). The MCMC sampler strongly preferred sinusoidal solutions to a top hat. In Figure 7, we plot a model set at the 2σ upper limit on the SPI

amplitude against the data, after subtracting the best-fit rotational modulation signal from those data.

The upper limit on the SPI signal enabled us to place a corresponding limit on the strength of the planetary magnetic field, under certain assumptions.

An initial assumption is that the magnetic disturbances from the planet propagate back to the star. For this to occur, the Alfvén Mach number at the planet must be <1 (Lanza 2015). Saur et al. (2013) estimated the Alfvén Mach number of GJ 436’s wind near GJ 436 b to be 1.01, very near the limit. This value relied on an empirically scaled estimate of the stellar wind speed at the planet of 235 km s^{-1} . In contrast, Bourrier (2016) estimate a lower value of 85 km s^{-1} , based on matching a model of the planetary outflow’s dynamical interaction with the stellar wind to Ly α transit data. This would imply an Alfvén Mach number ≈ 0.3 , making a magnetic SPI capable of propagating to the star. However, this still relies on an estimate of the stellar magnetic field that is based on a scaling relationship for Sun-like stars (Saur et al. 2013). A direct measurement of GJ 436’s magnetic field is necessary to better gauge whether GJ 436 b orbits within a region where the Alfvén Mach number is <1 .

A second assumption is that the interaction takes the form of the “flux tube dragging” scenario set forth by Lanza (2013). In this scenario, a persistent magnetic flux tube links the star and the planet. The orbital motion of the planet drags this tube through the ambient stellar magnetic field, triggering the stellar field to relax to lower-energy states, releasing energy in the process. This is the only SPI configuration that predicts energy release at a level that is consistent with past observations of stellar activity–related emission that is modulated at the orbital period of a close-in planet (Cauley et al. 2019). Note that for other SPI models, the relative orientation of the planetary and stellar fields can play a critical role (e.g., Strugarek 2016).

We followed the methodology of Cauley et al. (2019) to estimate an upper limit on GJ 436 b’s magnetic field. The method requires estimates for a number of quantities. For the stellar field at the planet, we took the value of 667 nT, as estimated by Saur et al. (2013). We set the relative velocity between the planet and the star’s magnetic field to be the same as the mean orbital velocity, estimated from the period and semimajor axis found by Lanotte et al. (2014). This simplification is justified, because the planet’s orbital velocity is over an order of magnitude larger than the rotational velocity of the stellar magnetic field at the orbital distance of the planet. We used the planetary radius value of $4.10 \pm 0.16 R_{\oplus}$ from Lanotte et al. (2014). Finally, to estimate the fraction of SPI power radiated in the summed FUV line flux, we used the flare energy budgets from panchromatic observations of stellar flares on the active M dwarf AD Leo, as reported by Hawley et al. (2003). These indicate that roughly 3% of the total energy that is emitted in a flare is emitted in the five lines that we summed. From the above values, we estimated an upper limit on the planetary magnetic field of $\lesssim 100 \text{ G}$. This limit is well above Jupiter’s magnetic field strength and within the range of values that Cauley et al. (2019) estimated for several hot Jupiters.

Besides inducing a hot spot, a close-in planet could affect the activity level of its host in several ways. It could suppress activity by tidally disrupting the stellar convective dynamo (Pillitteri et al. 2014; Fossati et al. 2018). It could obscure activity by enshrouding the star in absorbing gas from a radiation-powered planetary outflow (Fossati et al. 2013;

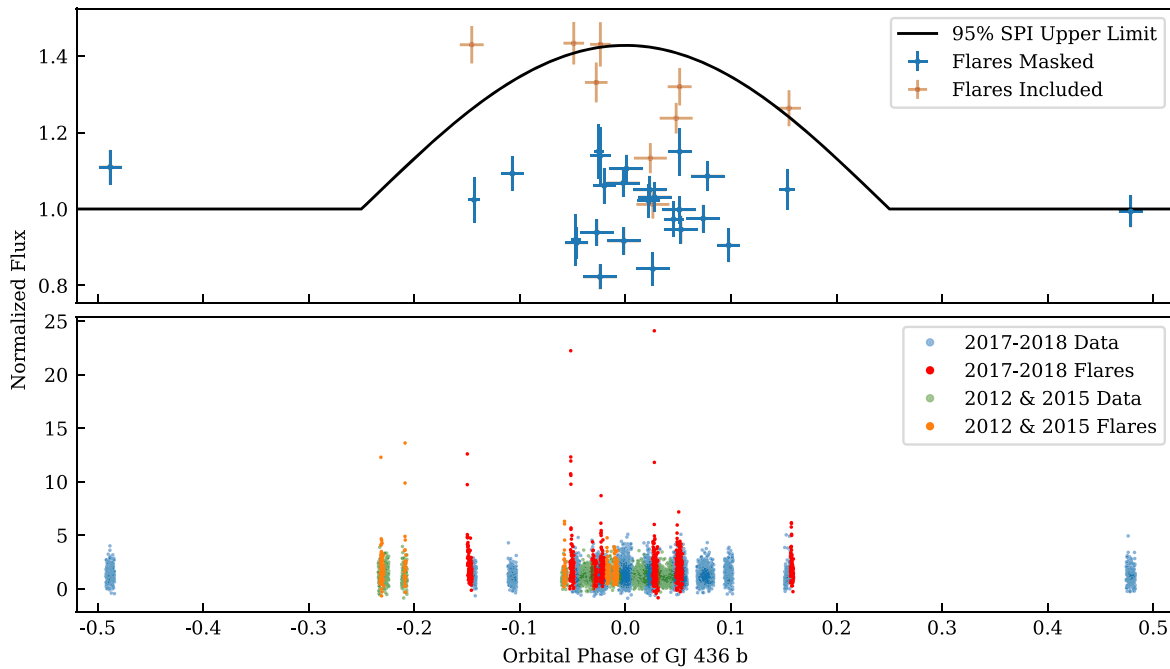


Figure 7. Fluxes plotted against planetary orbital phase. The planet’s optical transit spans a narrow range of ± 0.008 in phase. Top: data from the 2017/2018 epoch, binned by exposure, with the best-fit rotational modulation subtracted. The blue points exclude and the red points include flares. The black solid line shows the 2σ upper-limit amplitude for a truncated sine SPI model fit to the data with flares included. Bottom: data at a 10 s cadence, to show individual flares. The blue (quiescent) and red (flare) data are from the 2017/2018 epoch, whereas the green (quiescent) and orange (flare) data are from the earlier 2012 and 2015 epochs. We speculate that the lack of flares when the planet is near eclipse (phase 0.5) could suggest that a magnetic SPI is triggering the star’s frequent small flares, but with energies too weak to register as a detection using the truncated sine model.

Staab et al. 2017). Alternatively (or even concurrently), it could enhance activity, by tidally inhibiting the spin-down of the host star (Poppenhaeger & Wolk 2014; Tejada Arevalo et al. 2021). GJ 436’s activity, in the form of FUV emission lines, falls a factor of a few below the predicted level for an M star with a 44 day rotation period (Lloyd et al. 2021; Pineda et al. 2021), but is not an outlier. For comparison, the early M star GJ 832 has a slightly shorter rotation period (37.5 ± 1.5 days; Gorrini et al. 2022) and a similar level of FUV emission, yet radial velocity (RV) surveys have not revealed a close-in massive planet (Bailey et al. 2009; Gorrini et al. 2022). We conclude that GJ 436’s level of FUV emission is not strongly influenced by the presence of its warm Neptune, but that a magnetic SPI could nonetheless be present.

Although we did not detect an SPI in the form of orbit-modulated emission, we speculate that GJ 436’s odd FFD could indicate a magnetic SPI. The enhancement of relatively low energy (equivalent duration ≈ 500 s) flares and the statistically significant lack of more energetic events could indicate that a magnetic SPI is triggering frequent releases of magnetic energy at low levels, thereby preventing the buildup of stored energy that is necessary to give rise to the larger flares exhibited by other M dwarfs.

The stars in the comparison sample from L18, which produced stronger flares, are less prone to magnetic SPIs. Within the sample, eight of 10 (six of six in the inactive sample) are known to host planets (including GJ 436; see Section 3.1). None are as massive and as close-in as GJ 436 b, though several come to within about a factor of 2 in terms of mass or distance. The closest comparison is GJ 581 b, a planet with $M \sin i = 15.8 \pm 0.3 M_{\oplus}$ orbiting 0.040 au from its host (Robertson et al. 2014), versus GJ 436 b’s $25.4^{+2.1}_{-2.0} M_{\oplus}$ mass and 0.031 au distance from its host (Lanotte et al. 2014). For

the two stars without known planets, RV limits do not exclude planets like GJ 436 b (Bailey & White 2012; Kossakowski et al. 2022).

Consistent with an SPI hypothesis is the lack of flares during planetary eclipses, when a subplanetary hot spot on the star would be most likely to be invisible. The eclipse data are too brief for this difference to be statistically significant.

Theoretically, the increase in the time-averaged emission caused by SPI-triggered flares should also produce a detectable orbit-modulated signal. For this reason, we included the flux added by flares when fitting for a possible SPI signal. With the flares included, the MCMC sampler favors a slight increase in the emission within the -0.25 to 0.25 phase range, but it is marginal, with a likelihood ratio near unity. Within this phase range, the average flux (after removing the best-fit rotation and cycle variability) is 1.7σ higher than the two visits near the planetary occultation. With more data, changes in the flare rate with planet phase, variations in the time-averaged emission with planet phase, and FFD statistics could all lead to the confirmation or refutation of an SPI in this system. The present data hint that flare statistics might have the greatest quantitative power in identifying a magnetic SPI.

3.6. Variability Synopsis

To place each form of variability in context, we compare their amplitudes side by side in Figure 8. Each type of variability has its own time structure, so each type has its own definition of “amplitude.”

Flares do not have a well-defined amplitude, since they occur stochastically, with large variations in peak flux (Figure 4). As a metric for comparison, we adopted the time-averaged contribution of the observed flares to the star’s emission. This

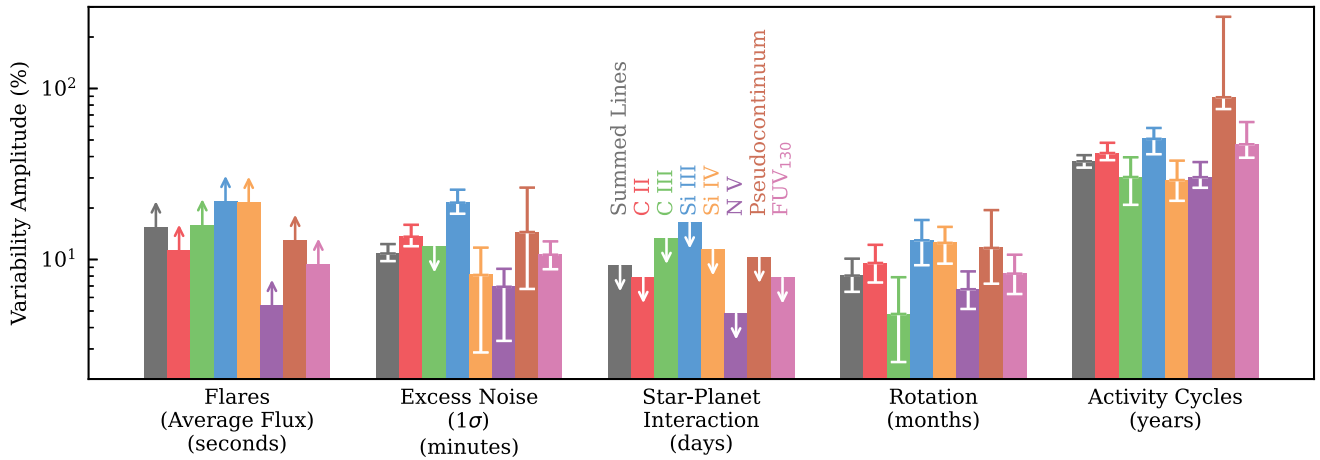


Figure 8. Summary of contributions from various sources to the FUV variability of GJ 436. The arrows indicate the upper or lower limits (see the text). In the parentheses below each label are the timescales at which we measured each form of variability.

number represents a lower limit on the true contribution of flares to the star’s time-averaged emission, because it omits both more frequent, weaker flares below the detection limit and larger, rarer flares that are not caught within the limited duration of the observations.

Excess noise, since we assumed it to be white noise, does not have time structure. However, better data could reveal structure on timescales of seconds to minutes that the present data do not resolve. As a metric for comparison, we adopted the 1σ level of the noise.

Our models for variability due to rotation, activity cycle, and SPI all have well-defined amplitudes. Since we did not detect SPI variations, Figure 8 shows only the 2σ upper limits on the amplitudes of the fits.

Activity cycles appear to be responsible for the greatest share of the variability observed across the observations. If the Sun is any guide, activity cycles will not only affect the average level of FUV emission, but also the frequency of flares and the amplitude of rotational variability. In other words, the amplitudes of other variability sources will wax and wane over the course of the stellar activity cycle.

The variability in most of the FUV bands that we considered is well correlated. Figure 9 plots the correlations between the fluxes of each pair of bands. For most line pairs, the points are consistent with a 1:1 correlation. The notable exceptions are N V and the pseudocontinuum. The variations in these bands, particularly at the high end (mostly due to flares), appear to be subdued, relative to the other lines, in line with the observations of M-dwarf flares (France et al. 2016; L18; France et al. 2020). Despite having a shallower slope for N V and the pseudocontinuum, correlations are still present at high significance in all cases, except the correlation between the pseudocontinuum and Si IV.

We expect the EUV emission of GJ 436 to track the changes in the FUV line fluxes. Bourrier et al. (2021) conducted differential emission measure modeling of the similar early M1.5 dwarf GJ 3470 across several observation epochs. From 2018 to 2019, GJ 3470’s FUV line fluxes increased by about 30%, while the flux in the 100–920 Å band predicted by differential emission measure distributions (DEMs) increased by about half of that, or 15%. In contrast, the Sun’s emission variability across activity cycles increases toward shorter wavelengths (Woods et al. 2022), suggesting the opposite

trend: that the variations in the EUV should exceed those in the FUV for GJ 436. France et al. (2018) also noted an effectively linear correlation between the Si IV and N V emission measured by HST and the 90–360 Å flux measured (at a different epoch) by the Extreme UltraViolet Explorer for a sample of 11 F–M dwarfs. Ultimately, simultaneous FUV–EUV observations of GJ 436 or similar stars are needed to quantify the relationship between FUV and EUV variability, but, at least qualitatively, EUV variations will track FUV variations. We leave DEM or stellar modeling reconstructions of GJ 436’s EUV emission to future work.

4. Summary

We conducted a comprehensive variability analysis of the FUV emission from the M2.5V exoplanet host star GJ 436. Our analysis has addressed flares, rotation, activity cycles, catch-all “excess noise,” and a possible SPI, with comparisons to the optical variability measured by Lothringer et al. (2018). We focused on the summed emission from the C II, C III, Si III, Si IV, and N V lines in the 1150–1450 Å range—the strongest lines in this range, aside from Ly α and O I, which were contaminated by geocoronal airglow.

Figure 8 provides a rapid comparison of the contribution of each variability source to the star’s overall variability. The star’s 2012–2018 activity cycle was responsible for the greatest degree of observed variability, $38\% \pm 3\%$ in amplitude. The observed flares increased the time-averaged emission by 15%. Any flares that were not observed, either because they were too weak to register above the noise or were too rare to be captured in the limited observing time, would add to this value. The star’s rotation produced variations of $8.1^{+2.1}_{-1.6}\%$, while a mixture of instrumental and astrophysical sources, treated with a catch-all white noise term, accounted for an additional $10.8^{+1.5}_{-1.1}\%$ variability in excess of photon noise. We did not detect any variability phased with the planet’s orbit, with a 2σ upper limit of 9.2%.

The uncertainty in the optical rotational phase at the time of the FUV observations precludes strong conclusions about the relative distributions of spots, faculae, and plage. Some other factors suggest that the star could be undergoing a transition from spot- to faculae-dominated activity, including the lack of reddening during optical minima, as found by Lothringer et al. (2018), the sinusoidal form of the star’s optical activity cycle, a

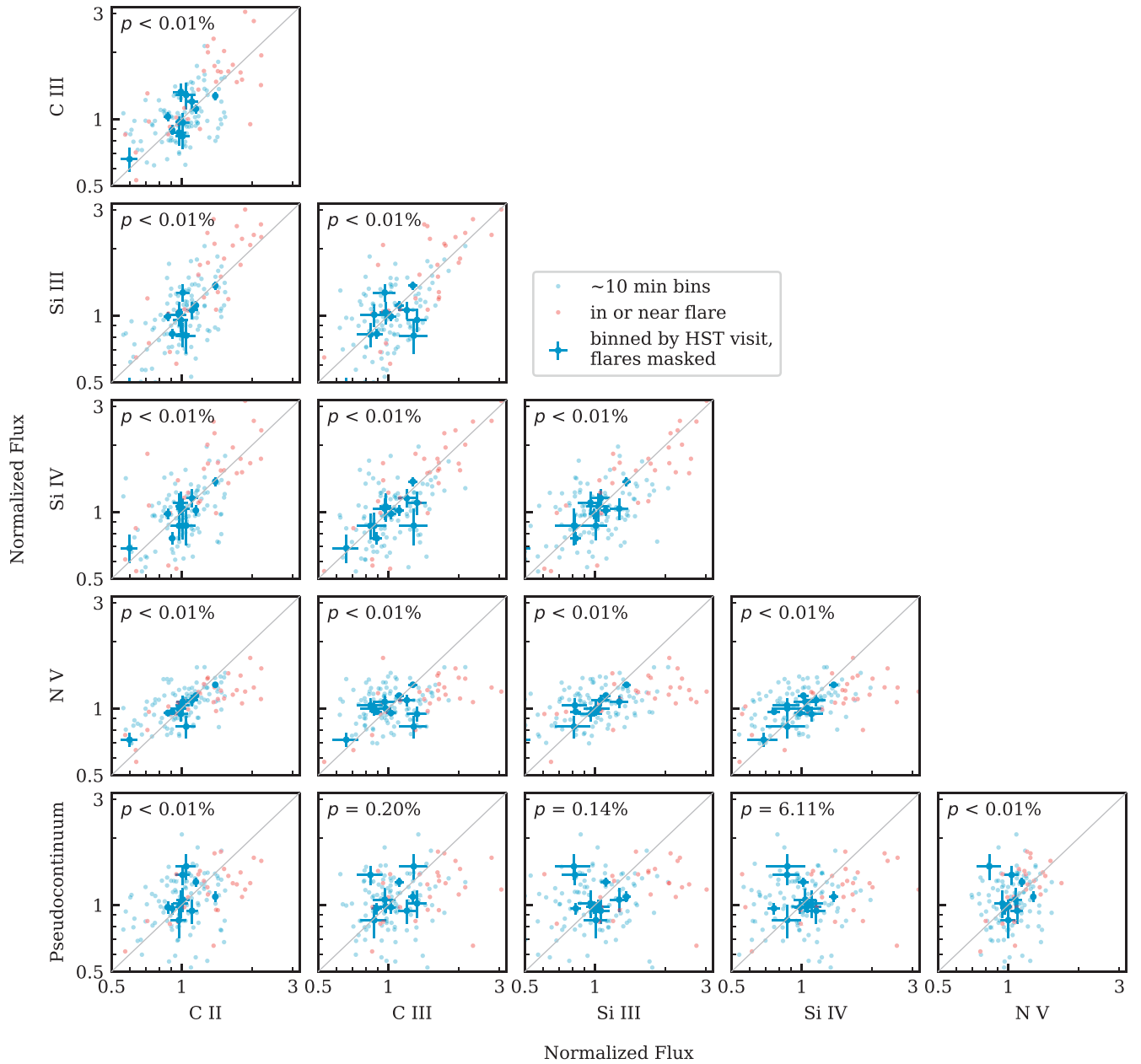


Figure 9. Correlations between the variability in each of the analyzed bands. The FUV₁₃₀ and summed line bands have been omitted, since they are compendia of all the other bands (thus not independent). The gray lines indicate a 1:1 correlation. The p -value from a Spearman rank order correlation test is given in each panel. Most band pairs are correlated to very high confidence, with the exception of some of the correlations with the pseudocontinuum. The largest excursions from the means are driven by flares, indicated by the red colorings of the points. Notably, neither NV nor the pseudocontinuum seem to follow 1:1 relationships with the other bands, although the statistical significances of the relationships remain very high, despite its shallower slope.

possible $119^\circ \pm 6^\circ$ phase offset between the optical and FUV cycles, and the star’s Rossby number near unity.

If the planet is magnetically interacting with its star, its magnetic field must have a strength $\lesssim 100$ G. Our upper limit on the SPI signal assumes that the variations appear as a truncated sine function, such as would be produced by a planet-induced hot spot traversing the stellar surface. However, the star produced an unusual population of flares that, we conjecture, could be the result of a magnetic SPI. Although the flares were numerous, totaling 12 (plus two dubious) events over the course of about a day of cumulative exposure, their energies were anomalously low in comparison to other M dwarfs. We speculate that this could result from a magnetic SPI triggering a multitude of flares with low equivalent

durations (a metric of flare energy normalized by the star’s quiescent flux). This would increase the flare rate at low equivalent durations, while disrupting the energy buildup necessary for stronger events. The lack of flares during planetary eclipse supports this view, but these visits were too brief to have statistical power.

The authors thank the anonymous referee for the thoughtful review and suggestions, as well as Antonio Lanza and Sebastian Pineda, for helpful discussions that improved this work. ROPL conducted this research under program HST-GO-15174. Support for program HST-GO-15174 was provided by NASA, through a grant from the Space Telescope Science Institute, which is operated by the Associations of Universities

for Research in Astronomy, Incorporated, under NASA contract NAS 5-26555. This research is based on observations made with the NASA/ESA Hubble Space Telescope, obtained from the Space Telescope Science Institute, which is operated by the Association of Universities for Research in Astronomy, Inc., under NASA contract NAS 526555. These observations are associated with program(s) 12646, 13650, 14767, and 15174.

Software: emcee (Foreman-Mackey et al. 2013), calCOS (<https://github.com/spacetelescope/calcos>), Astropy (Astropy Collaboration et al. 2013, 2018, 2022), NumPy (Harris et al. 2020), SciPy (Virtanen et al. 2020).

ORCID iDs

R. O. Parke Loyd  <https://orcid.org/0000-0001-5646-6668>
 P. C. Schneider  <https://orcid.org/0000-0002-5094-2245>
 James A. G. Jackman  <https://orcid.org/0000-0003-0711-7992>
 Kevin France  <https://orcid.org/0000-0002-1002-3674>
 Evgenya L. Shkolnik  <https://orcid.org/0000-0002-7260-5821>
 Nicole Arulanantham  <https://orcid.org/0000-0003-2631-5265>
 P. Wilson Cauley  <https://orcid.org/0000-0001-9207-0564>
 Joe Llama  <https://orcid.org/0000-0003-4450-0368>
 Adam C. Schneider  <https://orcid.org/0000-0002-6294-5937>

References

- Astropy Collaboration, Price-Whelan, A. M., Lim, P. L., et al. 2022, *ApJ*, **935**, 167
- Astropy Collaboration, Price-Whelan, A. M., Sipőcz, B. M., et al. 2018, *AJ*, **156**, 123
- Astropy Collaboration, Robitaille, T. P., Tollerud, E. J., et al. 2013, *A&A*, **558**, A33
- Bailey, J., Butler, R. P., Tinney, C. G., et al. 2009, *ApJ*, **690**, 743
- Bailey, J. I. I., & White, R. J. 2012, *ApJ*, **749**, 16
- Bourrier, V., dos Santos, L. A., Sanz-Forcada, J., et al. 2021, *A&A*, **650**, A73
- Bourrier, V., Lecavelier des Etangs, A., Ehrenreich, D., Tanaka, Y. A., & Vidotto, A. A. 2016, *A&A*, **591**, A121
- Bourrier, V., Lovis, C., Beust, H., et al. 2018, *Natur*, **553**, 477
- Bourrier, V., Zapatero Osorio, M. R., Allart, R., et al. 2022, *A&A*, **663**, A160
- Butler, R. P., Vogt, S. S., Marcy, G. W., et al. 2004, *ApJ*, **617**, 580
- Cauley, P. W., Shkolnik, E. L., Llama, J., & Lanza, A. F. 2019, *NatAs*, **3**, 1128
- Cuntz, M., Saar, S. H., & Musielak, Z. E. 2000, *ApJL*, **533**, L151
- Del Zanna, G., Dere, K. P., Young, P. R., & Landi, E. 2021, *ApJ*, **909**, 38
- Dere, K. P., Landi, E., Mason, H. E., Monsignori Fossi, B. C., & Young, P. R. 1997, *A&AS*, **125**, 149
- dos Santos, L. A., Ehrenreich, D., Bourrier, V., et al. 2019, *A&A*, **629**, A47
- Ehrenreich, D., Bourrier, V., Wheatley, P. J., et al. 2015, *Natur*, **522**, 459
- Foreman-Mackey, D., Hogg, D. W., Lang, D., & Goodman, J. 2013, *PASP*, **125**, 306
- Fossati, L., Ayres, T. R., Haswell, C. A., et al. 2013, *ApJL*, **766**, L20
- Fossati, L., Koskinen, T., France, K., et al. 2018, *AJ*, **155**, 113
- France, K., Arulanantham, N., Fossati, L., et al. 2018, *ApJS*, **239**, 16
- France, K., Duvvuri, G., Egan, H., et al. 2020, *AJ*, **160**, 237
- France, K., Froning, C. S., Linsky, J. L., et al. 2013, *ApJ*, **763**, 149
- France, K., Loyd, R. O. P., Youngblood, A., et al. 2016, *ApJ*, **820**, 89
- Fröhlich, C. 2006, *SSRv*, **125**, 53
- Gillon, M., Pont, F., Demory, B. O., et al. 2007, *A&A*, **472**, L13
- Gorini, P., Astudillo-Defru, N., Dreizler, S., et al. 2022, *A&A*, **664**, A64
- Granzler, T., Schüssler, M., Caligari, P., & Strassmeier, K. G. 2000, *A&A*, **355**, 1087
- Harris, C. R., Millman, K. J., van der Walt, S. J., et al. 2020, *Natur*, **585**, 357
- Hawley, S. L., Allred, J. C., Johns-Krull, C. M., et al. 2003, *ApJ*, **597**, 535
- James, B. L. 2022, *COS Instrument Handbook*, Vol. 14 (Baltimore, MD: Space Telescope Science Institute), 14
- Knutson, H. A., Madhusudhan, N., Cowan, N. B., et al. 2011, *ApJ*, **735**, 27
- Kossakowski, D., Kürster, M., Henning, T., et al. 2022, *A&A*, **666**, A143
- Kulow, J. R., France, K., Linsky, J., & Loyd, R. O. P. 2014, *ApJ*, **786**, 132
- Kumar, M., & Fares, R. 2023, *MNRAS*, **518**, 3147
- Lanotte, A. A., Gillon, M., Demory, B. O., et al. 2014, *A&A*, **572**, A73
- Lanza, A. F. 2013, *A&A*, **557**, A31
- Lanza, A. F. 2015, in 18th Cambridge Workshop on Cool Stars, Stellar Systems, and the Sun (Flagstaff, AZ: Lowell Observatory), 811
- Lavie, B., Ehrenreich, D., Bourrier, V., et al. 2017, *A&A*, **605**, L7
- Lothringer, J. D., Benneke, B., Crossfield, I. J. M., et al. 2018, *AJ*, **155**, 66
- Loyd, R. O. P., & France, K. 2014, *ApJS*, **211**, 9
- Loyd, R. O. P., France, K., Youngblood, A., et al. 2018b, *ApJ*, **867**, 71
- Loyd, R. O. P., Koskinen, T. T., France, K., Schneider, C., & Redfield, S. 2017, *ApJL*, **834**, L17
- Loyd, R. O. P., Shkolnik, E. L., Schneider, A. C., et al. 2018a, *ApJ*, **867**, 70
- Loyd, R. O. P., Shkolnik, E. L., Schneider, A. C., et al. 2021, *ApJ*, **907**, 91
- MacGregor, M. A., Weinberger, A. J., Loyd, R. O. P., et al. 2021, *ApJL*, **911**, L25
- Newton, E. R., Mondrik, N., Irwin, J., Winters, J. G., & Charbonneau, D. 2018, *AJ*, **156**, 217
- Pagano, I., Lanza, A. F., Leto, G., et al. 2009, *EM&P*, **105**, 373
- Pillitteri, I., Wolk, S. J., Sciortino, S., & Antoci, V. 2014, *A&A*, **567**, A128
- Pineda, J. S., Youngblood, A., & France, K. 2021, *ApJ*, **911**, 111
- Poppenhaeger, K., & Wolk, S. J. 2014, *A&A*, **565**, L1
- Reinhold, T., Bell, K. J., Kuzlewicz, J., Hekker, S., & Shapiro, A. I. 2019, *A&A*, **621**, A21
- Robertson, P., Mahadevan, S., Endl, M., & Roy, A. 2014, *Sci*, **345**, 440
- Sangal, K., Srivastava, A. K., Kayshap, P., et al. 2022, *MNRAS*, **517**, 458
- Saur, J., Grambusch, T., Duling, S., Neubauer, F. M., & Simon, S. 2013, *A&A*, **552**, A119
- Segura, A., Meadows, V. S., Kasting, J. F., Crisp, D., & Cohen, M. 2007, *A&A*, **472**, 665
- Shields, A. L., Ballard, S., & Johnson, J. A. 2016, *PhR*, **663**, 1
- Shkolnik, E., Bohlender, D. A., Walker, G. A. H., & Collier Cameron, A. 2008, *ApJ*, **676**, 628
- Shkolnik, E., Walker, G. A. H., & Bohlender, D. A. 2003, *ApJ*, **597**, 1092
- Staab, D., Haswell, C. A., Smith, G. D., et al. 2017, *MNRAS*, **466**, 738
- Strugarek, A. 2016, *ApJ*, **833**, 140
- Suárez Mascareño, A., Rebolo, R., & González Hernández, J. I. 2016, *A&A*, **595**, A12
- Suárez Mascareño, A., Rebolo, R., González Hernández, J. I., & Esposito, M. 2015, *MNRAS*, **452**, 2745
- Tejada Arevalo, R. A., Winn, J. N., & Anderson, K. R. 2021, *ApJ*, **919**, 138
- Toriumi, S., Airapetian, V. S., Hudson, H. S., et al. 2020, *ApJ*, **902**, 36
- Torres, G., Winn, J. N., & Holman, M. J. 2008, *ApJ*, **677**, 1324
- Virtanen, P., Gommers, R., Oliphant, T. E., et al. 2020, *NatMe*, **17**, 261
- Walker, G. A. H., Croll, B., Matthews, J. M., et al. 2008, *A&A*, **482**, 691
- Wheatland, M. S. 2000, *ApJL*, **536**, L109
- Woods, T. N., Harder, J. W., Kopp, G., & Snow, M. 2022, *SoPh*, **297**, 43